

Paper draft v1.7 for supersat project

K. Latimer

Feb 28, 2020

Questions/comments from DR in blue

Responses from KL in red

Hanging details to address before final draft

1 Intro

In a recent paper, Fan et al introduce a novel “warm phase invigoration mechanism” (WPIM) in which increased concentrations of ultrafine aerosol particles ($\text{UAP}_{<50}$, with 50 signifying an upper bound on particle diameter of 50nm) in the boundary layer (BL) result in enhanced convective updraft speeds and precipitation rates [1]. As pointed out by Grabowski and Morrison, the precise explanation for this physical effect is that, in allowing for lower equilibrium water vapor supersaturation (SS) values in rising convective parcels, these excess aerosol particles lead to an increase in the buoyancy of the parcel over the course of its ascent, thus enhancing convective speeds [2].

In order to get a quantitative intuition for how this works, we offer a simplified version of the calculation in [3], which still conveys the same essential idea. We consider a polluted (non-supersaturated; i.e. $RH = 1$) storm ascending in an environment whose temperature profile has been set by clean storms. The parcel condenses water vapor as it rises, and for simplicity we assume no latent heat is lost to the environment. We then have (see Table 1 for explanation of constants and variables used in the text. We use δ here to represent a variation in state variables between two parcels, as distinguished from d in Equation 5 which denotes a proper differential form):

$$C_{ap}\delta T + L_v\delta q_v = 0, \quad (1)$$

where q_v is the water vapor mass fraction of the parcel ($q_v = m_v/m_{tot}$), also expressed in terms of the relative humidity (RH) and saturation water vapor mass fraction (q_v^*) as:

$$q_v = RHq_v^* \quad (2)$$

Use the Clausius-Clayperon equation:

$$\begin{aligned}
\delta q_v^* &= \delta \left(\frac{e_s V}{R_v T m_{tot}} \right) \\
&= \frac{\delta e_s}{e_s} q_v^* - \frac{\delta T}{T} q_v^* \\
&= \frac{L_v \delta T}{R_v T^2} q_v^* - \frac{\delta T}{T} q_v^* \\
&= \left(\frac{L_v}{R_v T} - 1 \right) \frac{\delta T}{T} q_v^* \\
&\approx \frac{q_v^* L_v}{R_v T^2} \delta T
\end{aligned} \tag{3}$$

Taking the differential of Equation 2 and rearranging terms in Equations 1, 2, and 3 yields:

$$\delta T = \frac{-L_v q_v^*}{C_{pa} + q_v \frac{L_v^2}{R_v T^2}} \delta RH \tag{4}$$

Plugging in typical values for RH (≈ 1.1) and T (≈ 300 K) gives $dT \approx 1$ K.

In their paper (see for example Figure 2(b) of that work), Fan et al provide anecdotal evidence that the WPIM is capable of producing enhancements in vertical wind velocity on the order of 10 m/s for polluted relative to unpolluted storms. Even neglecting diffusive, frictional, or radiative losses, this requires a variation in convective available potential energy ($CAPE$) of ≈ 100 J/kg, or a RH difference between the dirty storm and clean environment of ≈ 0.1 , i.e., the environment must support SS on the order of 10% throughout the troposphere.

While Fan et al do not offer any proof based on experimental data that such high SS exist in the convection setting the environmental lapse rate, they do observe comparable values in numerical simulations. In particular, using the Weather Research and Forecasting (WRF) model to simulate pristine (no $UAP_{<50}$) conditions in the Amazon Rainforest, they find (horizontally- and time-averaged) SS in convective cores of up to 15%.

Since this is well above what is typically reported or assumed in the literature [4, 5, 6, 7, 8, 9, 10, 11, 12], we seek in this paper to determine if we can find experimental evidence for $O(10\%)$ SS in nature. We use data from the High-Altitude Long-range research aircraft (HALO) (part of the ACRIDICON-CHUVA mission in and around Manaus, Brazil in 2014-15), as well as from the first phase of the Cloud Aerosol Interaction and Precipitation Enhancement Experiment (CAIPEEX) in India (taken in June [around Hyderabad] and August [around Bareilly] 2009) [?, 14] as a dataset of opportunity.

2 Data Analysis and Results

In order to determine experimental supersaturation within a reasonable margin of error, we must use the quasi-steady-state supersaturation (SS_{QSS}) formula

[15]. In order to determine the region of validity for this approximation, we used data from the WRF output, since this allows us to compare to the true supersaturation (here called SS_{WRF}). We focused on the following considerations:

- The QSS approximation should be a good and reliable estimate for the actual SS, i.e. least-squares linear regression slope and correlation coefficients ≈ 1 .
- We want the criteria to be inclusive enough that we are still capturing a significant fraction of the convection which sets the average temperature profile of the troposphere.
- In keeping with the analysis by Fan et al, and with our general interest in studying convective cores, we additionally exclude the w lower bound value of 0 to ensure we are capturing reasonably strong updrafts.

In Figure 1 we synthesize the data needed to take all three of the above considerations into account. We find that taking $LWC > 10^{-4}$ kg/kg and $w > 1$ m/s yields the best agreement of the QSS approximation with the true SS while still yielding a subset of the data that accounts for greater than half of the condensational latent heating in the troposphere below the freezing line and consists of reasonably strong convective updrafts. To summarize, we use the following criteria in all subsequent analyses:

- $T > 273K$ (we’re not including ice in the theory; note that Fan et al do evaluate SS wrt water above the freezing line though)
- $w > 1$ m/s
- cloud $LWC > 1e-4$ g/g (in the convection core)
- including rain droplets and ventilation corrections

We would like to further quantify the spread of true SS values for a given value predicted by the QSS approximation. In Figure 2, we plot a range of quantiles for the true SS given the predicted SS, using the polluted and unpolluted data sets combined (see Table ?? for details on the regression parameters for each case).

In their analysis, Fan et al use the following filtering criteria:

- For experimental data: They examine the upper 10th percentile of updrafts in “convective events” which 1) Fall between 11h00 and 19h00 local time 2) Have no other convective events occurring at any point in time 3 hours prior, and 3) Have max echo height at $> 0dBz$ above 10km. For aerosol measurements they take the average of measurements in the 30-min interval prior to the convective event. The authors do not state their criteria for what qualifies as a convective event.

- For model data: They limit analysis to a subset of the horizontal domain (red box in Fig S8) that encompasses a single convective event during the day of the simulation. They again take the top 10th percentile of updrafts with $w > 2$.

Because we use slightly different filtering criteria than that described above, we first verify that the data points selected by our filter yield similar SS profiles in the WRF simulation as those found in the latter work. In Figure 3 we plot vertical SS profiles for all filtered data points, as well as for the upper 10 percentiles of all filtered data points. We define the points in the “upper 10 percentiles” as those with w greater than the 90th-percentile (out of all altitudes and times) vertical wind velocity. Data in Figure 3 are binned according to the simulation grid, which is based on pressure coordinates so that bin size varies logarithmically with respect to z . For this and future vertical profiles, the vertical coordinate of plotted points represents the average over all vertical coordinates of points in the corresponding bins. In [1] they consider a restricted subdomain around the T3 field station, indicated in Figure S8 of the supplementary information for that paper; we do not see a major qualitative difference when including this additional criterion; see Figure 15. We do indeed find the high SS values reported by Fan et al (maximum values of 13% in both polluted and unpolluted cases from the upper 10th percentile dataset), confirming that our filtering criteria establish a fair basis for comparison here.

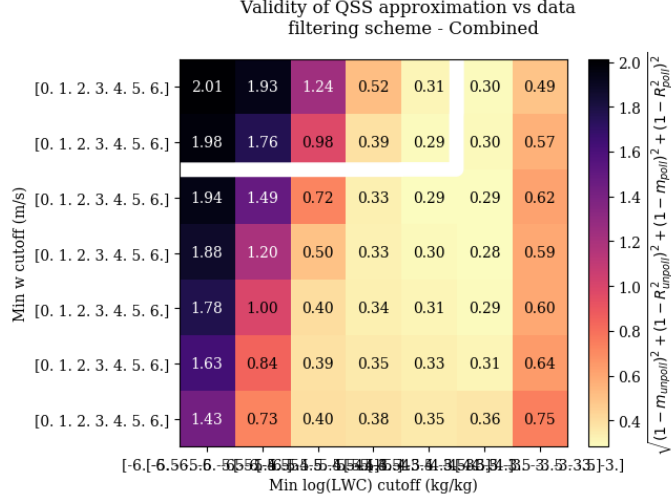
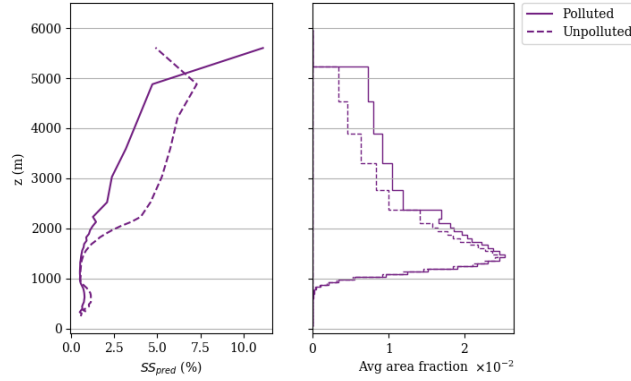


Figure 1: Systematic evaluation of data filtering scheme using WRF model outputs. Here, the heatmap color corresponds to the Euclidean distance in the 4-dimensional space of tuples $(m_{poll}, R_{poll}^2, m_{unpoll}, R_{unpoll}^2)$ from the ideal point $(1, 1, 1, 1)$, where subscripts ‘poll’ and ‘unpoll’ correspond to Fan et al’s ‘C_PI’ (polluted) and ‘C_BG’ (unpolluted) model scenarios, respectively. Numerical values of this distance are also given as annotations to aid in distinguishing similar colors. Values on the horizontal and vertical axes represent, respectively, minimum LWC and w cutoffs used to filter WRF simulation data. In all cases we additionally restrict our consideration to points with temperature above 273 K. We also seek to evaluate the fraction of domain-wide positive (i.e. condensational) latent heating attributed to points selected through the data filter. The higher the fraction, the more confidence we have (in an unquantified sense) that we are capturing a complete picture of the convection which sets the temperature profile in the troposphere. The white contour line indicates the region of the heatmap where the LH fraction is $> 50\%$ for both polluted and unpolluted model scenarios.



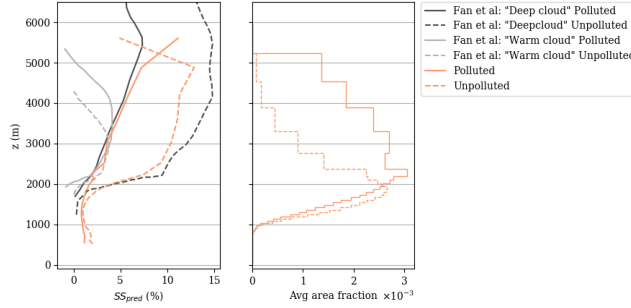
Figure 2: This figure shows the spread of true SS values for a given value predicted by the QSS approximation, using the combined WRF output from both polluted and unpolluted models. Each curve follows a fixed quantile (labeled on the figure) across the domain of predicted SS values for the range of actual SS. The quantiles are calculated with a 0.01-wide moving window centered on the respective predicted value. We see that the actual SS hew closely enough to the predicted SS that a high predicted SS guarantees a high actual SS, and vice versa. Up to about a QSS SS of 0.1, the median actual SS is, to good approximation, equal to the predicted SS. From this plot we can simply read off the confidence level of our lower bound on actual SS; for example, for a single predicted SS of 0.1, there is 95% confidence that actual SS < 0.14 .

Supersaturation and area fraction vertical profiles - WRF Unpolluted



(a)

Supersaturation and area fraction vertical profiles - WRF Unpolluted



(b)

Figure 3: This figure serves to verify that our data filtering scheme yields SS profiles similar to those obtained by Fan et al (c.f. Figure 4 of that paper). Using a) all filtered data points and b) only the top 10 percentiles of filtered data points as measured by w (see text for details), the latter being aligned with the analysis method of Fan et al. Left hand panels show SS_{QSS} averaged across time and horizontal spatial coordinates. Right hand panels show time-averaged area fraction occupied by filtered data points. Note that z interval width scales logarithmically with z , in accordance with the WRF grid spacing. The gray curves in (b) are reconstructed from [1]; ‘warm cloud’ and ‘deep cloud’ designate early and central periods of precipitation measured by surface rain rates (our analysis does not make that distinction). We observe that our filtering scheme indeed recovers average SS_{QSS} values on the order of 10% as reported in [1]. The dropoff in area fraction in (a) at higher altitudes is due to a fairly sharp peak in LWC around 2 km (see Figure ?? in Supplementary section).

We now seek to determine whether such high values actually occur in nature. First we look at data from the HALO flights in September and October of 2014 (see Methods/SI for details on selection of dates for this analysis) [[find citation](#)]. Figure 4 shows the analogue of Figure 3 using data from all HALO flight dates combined. We find no points with average SS above 1 %, even when limiting to the strongest updrafts in the combined dataset.

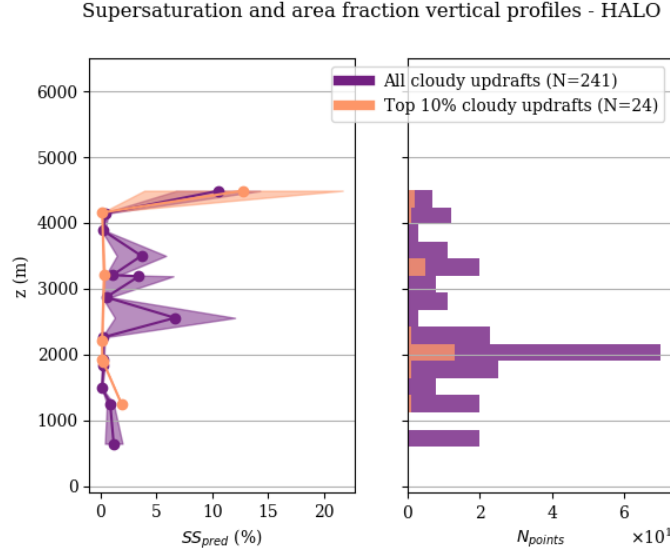


Figure 4: This figure serves to determine whether the high-SS values found in the WRF simulation output indeed occur in nature. Left hand panel shows SS_{QSS} averaged across all filtered data points from HALO flight campaign (all dates combined), as well as across only the top 10 percentiles of those filtered data points as measured by w (see text for details). Right hand panel shows the number of points in each z interval (constant with respect to z) used in the analysis. We do not find any points in the SS_{QSS} profile with values above 1%, even when restricting to only the top 10 percentiles.

Finally, we examine a second experimental dataset from the first phase of the CAIPEEX campaign [14]. Although no $UAP_{<50}$ concentration measurements are available during this phase of the experiment, measurements of aerosols with diameters in the range of $0.1\text{--}3\text{ }\mu\text{m}$ showed total aerosol concentrations ranging from 700/ccm to 2500/ccm in the BL (see Figure 3(b) in [16] and Figure 4(a) in [14]). Reliable rain drop particle size distributions are unavailable from the flight dates in this analysis phase of the experiment, but we observe that exclusion of raindrops from the calculation of QSS SS leads to a systematic overestimation of the true SS (see Methods/SI). Therefore we take the SS profiles in Figure 5 as an upper bound. We observe slightly higher values relative to those from the HALO flights, although we still don't find such high values as those output by

the WRF models for the middle troposphere.

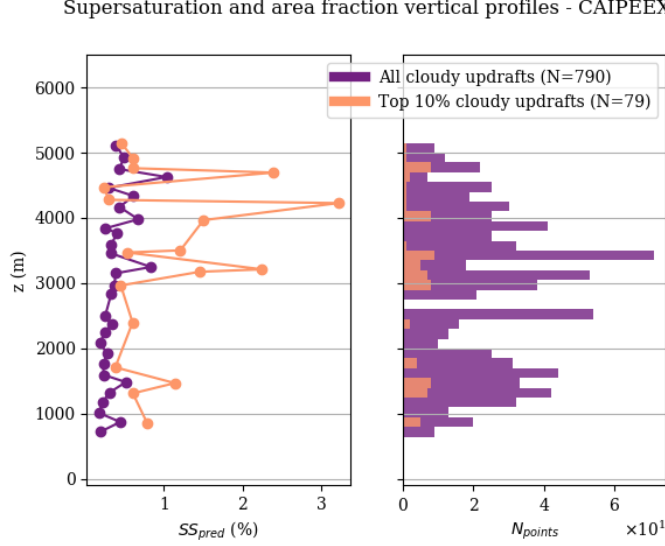


Figure 5: Analogous to Figure 4 but using experimental data from the CAIPEEX flight campaign. The only difference in the analysis for this dataset (relative to for the HALO dataset) is that we did not have access to size-resolved rain drop spectra (see text for detailed discussion). We do not find any points in the SS_{QSS} profile with values above 2% for the entire filtered data set, with only one point in the profile exceeding 3% for the top 10 percentiles.

We can use Equation 4 and the SS profiles in Figures 3-5 to infer a buoyancy profile for a hypothetical non-supersaturated parcel. For this analysis we take the temperature of the parcel equal to that of the environment (i.e., what has been measured). The resulting error in the value of δT in Equation 5 is quadratic in δRH , which is acceptable for our purposes. In Figure 6 we plot δT profiles from both WRF simulations and field campaigns side-by-side. We use these profiles to derive enhancements in $CAPE$ for the non-supersaturated parcel as:

$$\delta CAPE = g \int dz \frac{\delta T}{T} \quad (5)$$

where we again approximate T as the environmental temperature and integrate from 647 to 4488 m, the common vertical domain for all four curves in Figure 6. We find values of $\delta CAPE$ of 3, 5, 30, and 50 J/kg for HALO, CAIPEEX, WRF (polluted), and WRF (unpolluted), respectively. Neglecting any other physical energy sinks as above, these translate to vertical velocity enhancements on the order of 1 m/s in the field campaigns and 10 m/s in the simulations.

One possible counterargument is that the aerosol concentrations in the BL during the dates of the HALO flights might have been significantly higher

than those during the dates considered in Fan’s paper, thus precluding the occurrence of high SS values in the troposphere. In order to investigate this, we use the aerosol particle size distribution measured by the scanning mobility particle sizer (SMPS) in Manacapuru, located southwest of Manaus (PI: Chongai Kuang). This instrument measures particle concentrations in the diameter range 11.1-469.8nm. In Figure 7, we show that, while we do indeed see higher total aerosol concentrations on average during the HALO flight date range (3500/ccm vs 2400/ccm), the UAP50 concentration is on average lower (670/ccm vs 1600/ccm). In fact, the aerosol concentrations used in the WRF simulations are much lower than those observed during the day the simulation takes place, which is not justified quantitatively in that study.

We note additionally that the positive experimental correlation between concentration of UAP50 and maximum vertical velocity during the dates studied by Fan et al is not significant at the 95% confidence level - the least-squares slope parameter for their data set (the plot of which we reproduce in Figure 8, with additional 95% confidence bands) has a p-value of 0.11.

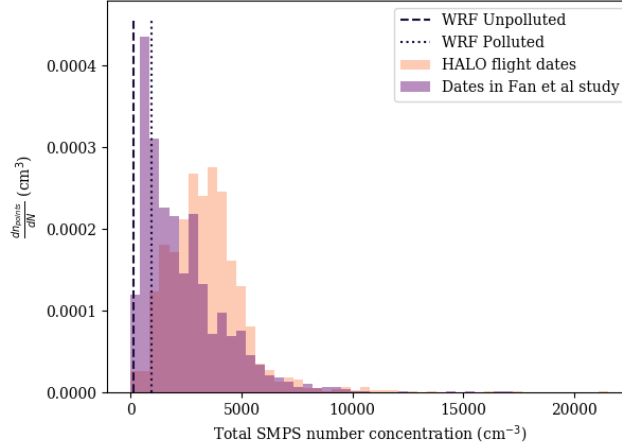
Another possible counterargument is that the flight campaigns simply didn’t fly through strong enough updrafts. However the vertical velocity distributions from the campaigns are quite similar to that from the simulations. See Figure 9.

Conclusion: The WPIM as proposed by Fan et al requires the average temperature profile of the troposphere to be set by relatively clean (high-SS) convection, in order for more polluted (low-SS) convection to experience an enhancement in buoyancy. However, we find no evidence that the high SS values reported by Fan’s model actually occur in nature, which weakens the possibility of measureable invigoration effects - in particular, we estimate an upper bound on vertical velocity enhancement of ≈ 1 m/s from the HALO and CAIPEEX flight campaigns, compared to ≈ 10 m/s from Fan’s control simulations in WRF. The relatively low aerosol concentrations used to initialize the simulations, in combination with possible irregularities in microphysical parameterizations, may be to blame for the anomalously high SS values in the WRF output.



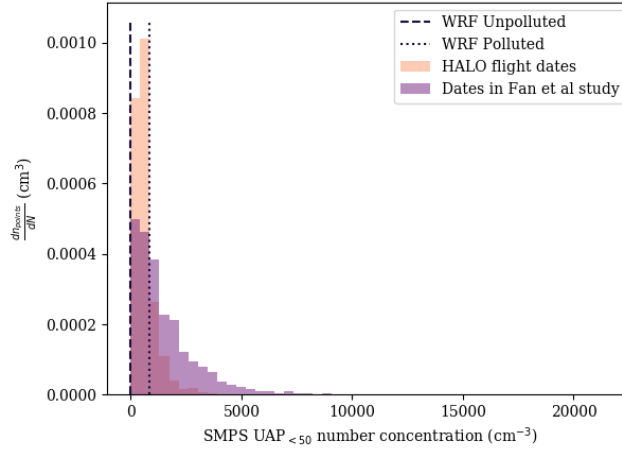
Figure 6: Profiles for δT of a non-supersaturated ($RH = 1$) parcel ascending in an environment with SS profiles shown in Figures 3-5, using Equation 5. SS profiles for HALO and CAIPEEX are plotted with markers so as not to obscure intervals with missing data. We find that the buoyancy of this hypothetical parcel in nature is far lower than in the simulations, casting doubt on the real validity of the WPIM as described in Fan et al.

Aerosol concentration distributions - 11.1-469.8 nm



(a)

Aerosol concentration distributions - 11.1-50 nm



(b)

Figure 7: Distribution of aerosol concentration measurements by the ground-based SMPS at Manacapuru, Brazil; a) entire size range, b) only particles with diameter greater than 50nm. HALO flight dates are the same as those represented in Figure 4 (see main text for details). Dashed (dotted) lines show initial concentrations in the BL of the WRF simulation of polluted (unpolluted) conditions. The unpolluted model aerosol concentrations are quite low relative to what is actually observed.

Max vertical wind velocity versus aerosol number concentration
(Reconstructed from reference [1])

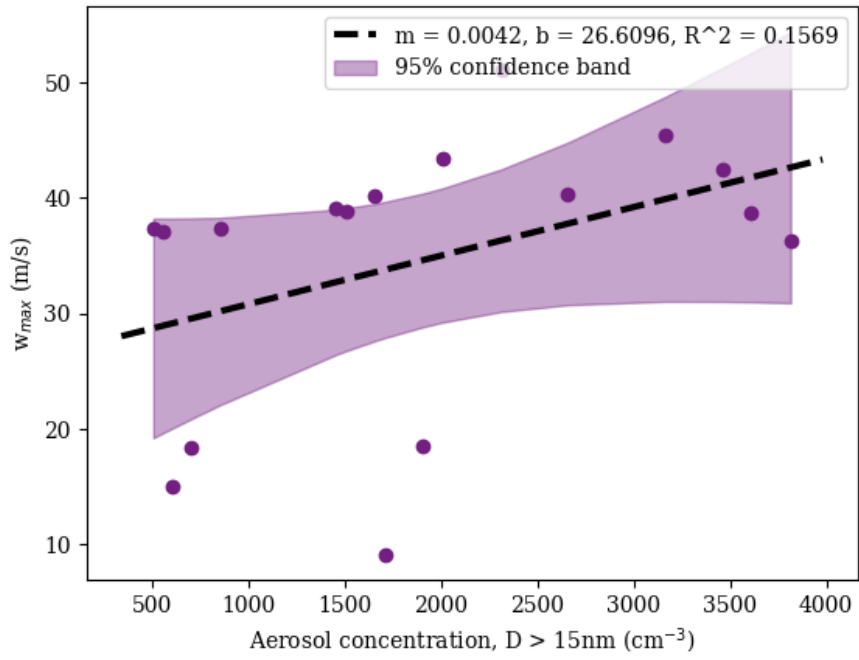


Figure 8: Ground-based total (including UAP50) aerosol concentration measurements versus maximum vertical wind velocity in convective cores; reproduced from Figure S2(a) of [1] with additional confidence bands our own. Note that a line with zero slope lies well within the confidence bands, corroborating the statistically insignificant p-value of the least-squares linear regression slope parameter.

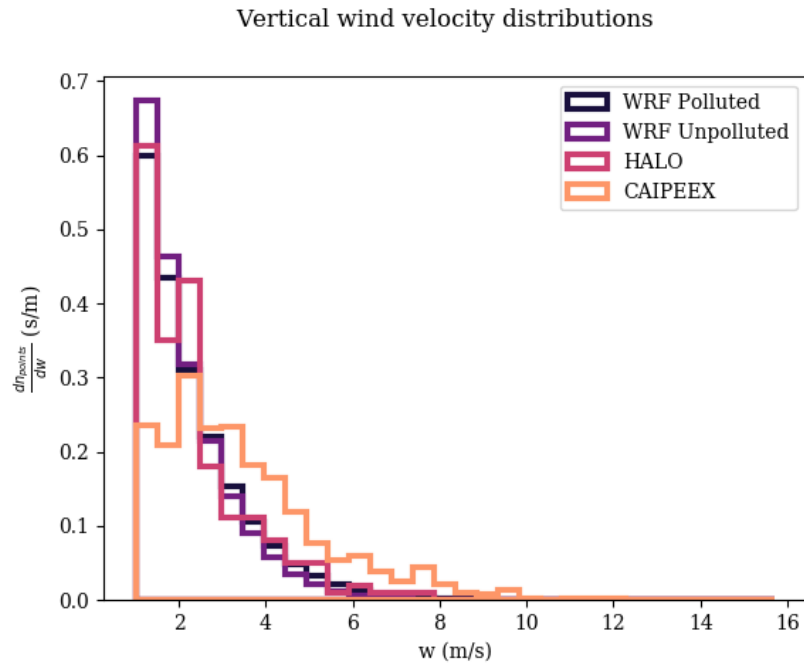


Figure 9: Vertical wind velocity probability distributions from simulations and field campaigns, using filtering criteria outlined in the text. Experimental distributions are not qualitatively different from those in the simulation.

3 Methods

3.1 WRF

Model output for control simulations of polluted (“C_BG”) and unpolluted (“C_PI”) scenarios were provided by Fan et al; see that paper and accompanying SI for detailed explanations of model parameters and initializations.

In this paper, we use the following form of the QSS SS equation after [15] (with SS_{QSS} given as a percentage):

$$SS_{QSS} = \frac{A(T)w}{4\pi B(\rho_a, T)\langle f(r) \cdot r \rangle n} * 100, \quad (6)$$

where:

$$\begin{aligned} A(T) &= \frac{g}{R_a T} \left(\frac{L_v R_a}{C_{ap} R_v T} - 1 \right) (F_d(T) + F_k(T)) \\ F_d(T) &= \frac{\rho_w R_v T}{De_s(T)} \\ F_k(T) &= \left(\frac{L_v}{R_v T} - 1 \right) \frac{L_v \rho_w}{KT} \\ B(\rho_a, T) &= \rho_w \left(\frac{R_v T}{e_s(T)} + \frac{L_v^2}{R_v C_{ap} \rho_a T^2} \right) \end{aligned} \quad (7)$$

Notation for constants and variables is given in Table 1. We use the following parameterization for e_s [15]:

$$e_s(T) = 611.2 e^{\frac{17.67T_c}{T_c + 243.5}}, \quad (8)$$

where T_c is the temperature in degrees Celsius.

We note that this equation by also include finite size correction terms; however, using typical values for droplet salinity and condensation nucleus radius (the relevant parameters in this case), these terms are insignificant ($< 0.1\%$ correction to SS) for drops of radius greater than $3 \mu\text{m}$ [15], and we therefore do not consider them in this paper.

A simpler form of Equation 6 is often employed in the literature [2, 15], with:

$$\begin{aligned} A(T) &= \frac{g}{R_a T} \left(\frac{L_v R_a}{C_{ap} R_v T} - 1 \right) \\ B(T) &= D \end{aligned} \quad (9)$$

Figure 12 shows that this form does not yield as good of agreement with the actual SS reported in WRF.

We use the expressions given in [17] and [15] for ventilation corrections, which are quite extensive. Full formulae are contained in the analysis code at this GitHub repo. Figures 13 and 14 show, respectively, the effects of neglecting these corrections (i.e. setting $f(r) = 1$ for all r) for rain drops (defined here as liquid water drops with diameter greater than $50 \mu\text{m}$), and omitting rain drops altogether from the calculations of mean radius and number concentration.

3.2 HALO

The HALO aircraft supported two instruments for measuring cloud droplet spectra: a cloud and aerosol spectrometer (CAS-DPOL) and a cloud droplet probe (one element of a cloud combination probe) (CCP-CDP) [18]. We found that the CCP-CDP consistently reported unphysical bimodal size distributions, and therefore used only data from the CAS-DPOL for all calculations involving cloud droplets. Number concentrations from the CAS-DPOL were corrected using the ξ factor derived in [19].

The rain drop spectra came from data collected by greyscale cloud imaging probe (second element of the cloud combination probe) (CCP-CIP). The drop diameter detection ranges for CAS-DPOL and CCP-CIP were 0.89-50 μm and 25-2000 μm , respectively. Per guidance from the principal investigators for the CAS-DPOL, we only included data for droplets from size bins with a lower diameter bound greater than 3 μm in the analysis [20]. Effectively (given size bins for this instrument), this meant that the lower bound on diameter for water drops was 5 μm . Because the CAS-DPOL and CCP-CIP have overlapping diameter detection ranges, we use concentrations for particles between 5 and 25 μm from CAS-DPOL and from 25 to 2000 μm from CCP-CIP.

All measurements of environmental variables were taken from the Basic Halo Measurement and Sensor System (BAHAMAS).

Out of the dates for which all three instruments (BAHAMAS, CAS-DPOL, CCP-CIP) report data, we take those for which measurements of shared variables (true airspeed for BAHAMAS and CAS-DPOL; ξ correction factor for CAS-DPOL and CCP-CIP) are well-correlated (R^2 above 0.95). These are (all in 2014): 6, 9, 11, 12, 16, 18, 27, 28, 30 September; 1 October.

We used the same Equation 6 for SS_{QSS} and for ventilation factors as described above.

3.3 CAIPEEX

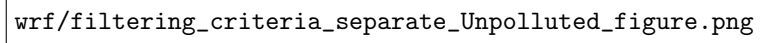
Cloud droplet spectra for phase 1 of the CAIPEEX field campaign were measured by a CDP (detection range 2-1562.5 μm). We used the data from the following flight dates in 2009: 16, 21, 22 June; and 18, 23, 24, 25 August.

We used the same Equation 6 for SS_{QSS} and for ventilation factors as described above, and excluded data from cloud droplets of diameter less than 5 μm .

4 Supplementary

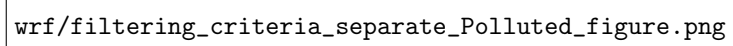
Symbol	Meaning	Value of constant	Notes
C_{ap}	Specific heat capacity at constant pressure, dry air	1005 J/kg	
D	Molecular diffusion constant of water in dry air	$0.23\text{e-}4 \text{ m}^2/\text{s}$	We take as constant wrt T
e_s	Saturation vapor pressure, water	-	
$f(r)$	Ventilation factor	-	
g	Gravitational acceleration on Earth	9.8 m/s	
K	Coefficient of thermal conductivity in dry air	$2.4\text{e-}2 \text{ J}/(\text{m s K})$	We take as constant wrt T
LWC	Liquid water content	-	
L_v	Latent heat of vaporization, water	$2.501\text{e}6 \text{ J/kg}$	We take as constant wrt T
N	Particle number concentration	-	
n_{points}	Point probability density	-	
q_v	Water vapor mass mixing ratio	-	Equals $\frac{m_w}{m_{tot}}$
q_v^*	Saturation water vapor mass mixing ratio	-	Equals $\frac{m_w^*}{m_{tot}}$
r	Particle radius	-	
RH	Relative humidity	-	Equals $SS + 1$
ρ_a	Mass density, dry air	-	Assuming ideal gas law
ρ_w	Mass density, liquid water	1000 kg/m ³	
R_a	Ideal gas constant, dry air	287.19 J/(kg K)	
R_v	Ideal gas constant, water	460.52 J/(kg K)	
SS	Supersaturation	-	Equals $RH - 1$
T	Temperature	-	
T_c	Temperature in degrees C	-	Equals $T - 273.15$
w	Vertical wind velocity	-	
z	Altitude	-	

Table 1: Explanation of constants and variables used in the paper.

A large rectangular box containing the text 'wrf/filtering_criteria_separate_Unpolluted_figure.png'. This box represents the visual output of the WRF model for the unpolluted case, showing filtering criteria.

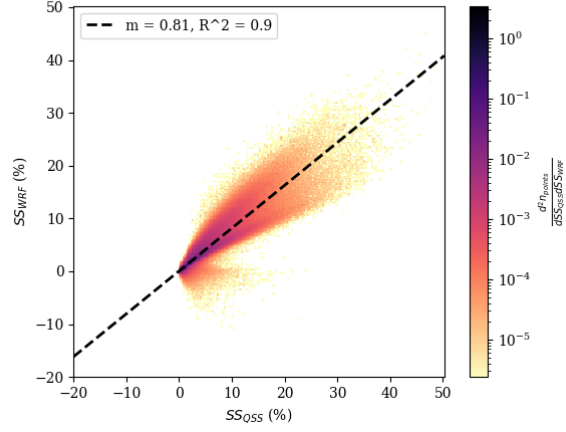
wrf/filtering_criteria_separate_Unpolluted_figure.png

(a) Unpolluted case.

A large rectangular box containing the text 'wrf/filtering_criteria_separate_Polluted_figure.png'. This box represents the visual output of the WRF model for the polluted case, showing filtering criteria.

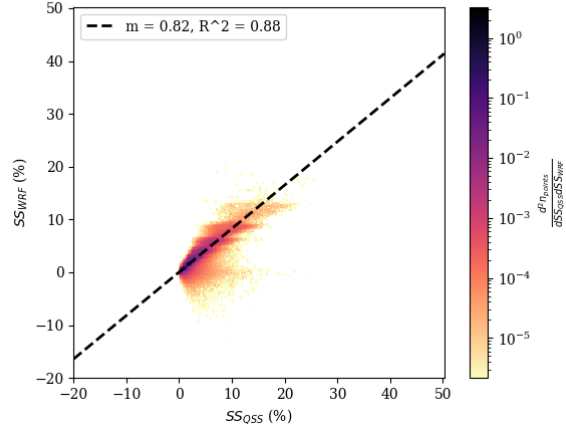
wrf/filtering_criteria_separate_Polluted_figure.png

Actual versus approximated supersaturation - WRF Unpolluted



(a) Unpolluted case.

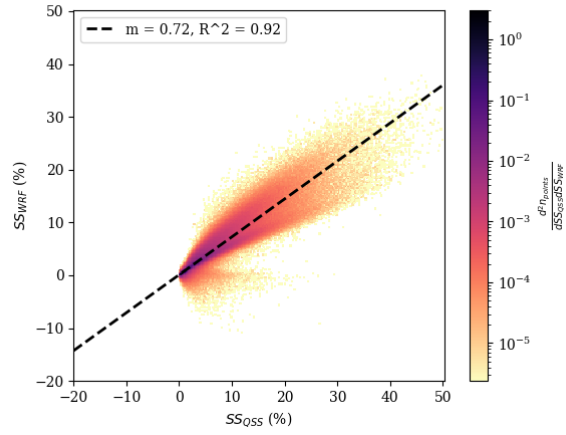
Actual versus approximated supersaturation - WRF Polluted



(b) Polluted case.

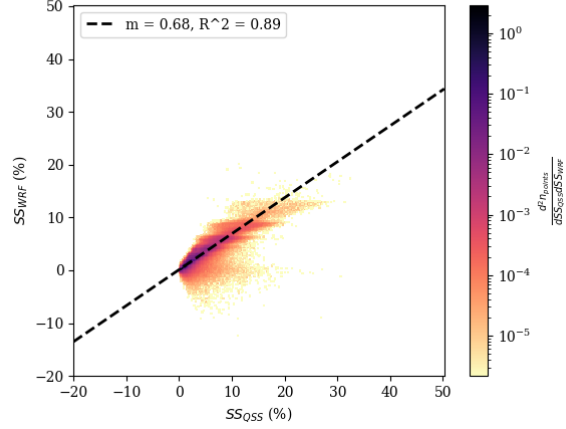
Figure 11: Plot of SS_{QSS} versus SS_{WRF} using the filtering scheme described in the main text. Dashed line shows the fit from least-squares linear regression. Color denotes the density of data points; note the scale is logarithmic in this figure. The majority of points are clustered near the origin.

Actual versus approximated supersaturation - WRF Unpolluted



(a) Unpolluted case.

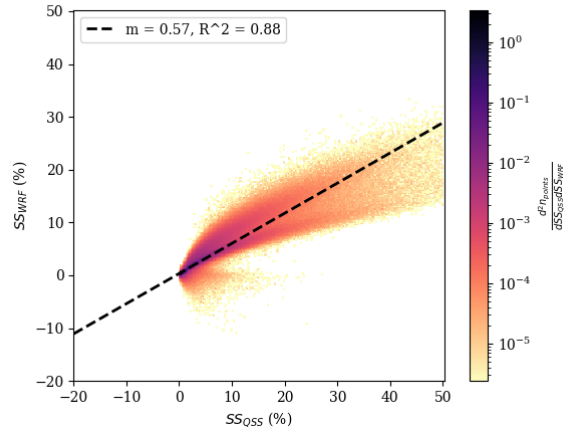
Actual versus approximated supersaturation - WRF Polluted



(b) Polluted case.

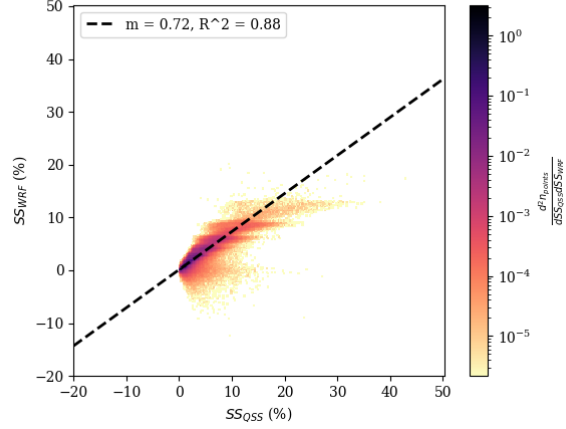
Figure 12: Same as Figure 11, using simplified form of Equation 6. Correlation is not appreciably affected but the value of least-squares linear regression slopes is lower for both simulation cases.

Actual versus approximated supersaturation - WRF Unpolluted



(a) Unpolluted case.

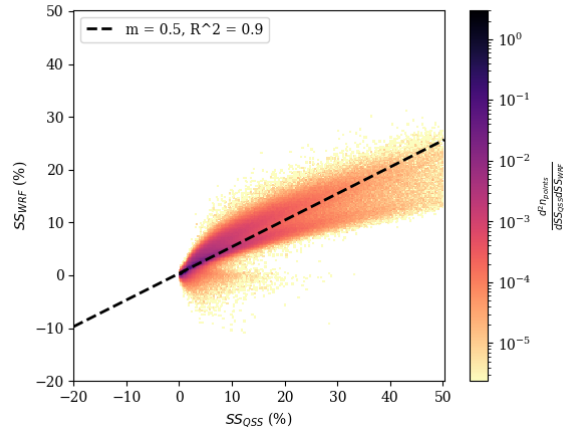
Actual versus approximated supersaturation - WRF Polluted



(b) Polluted case.

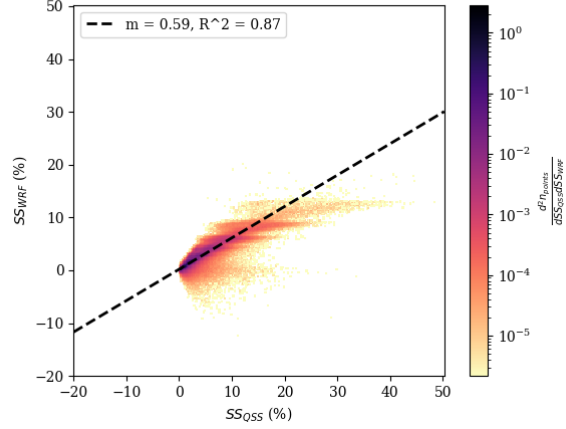
Figure 13: Same as Figure 11, without ventilation corrections. Correlation is not appreciably affected but the value of least-squares linear regression slopes is lower for both simulation cases.

Actual versus approximated supersaturation - WRF Unpolluted



(a) Unpolluted case.

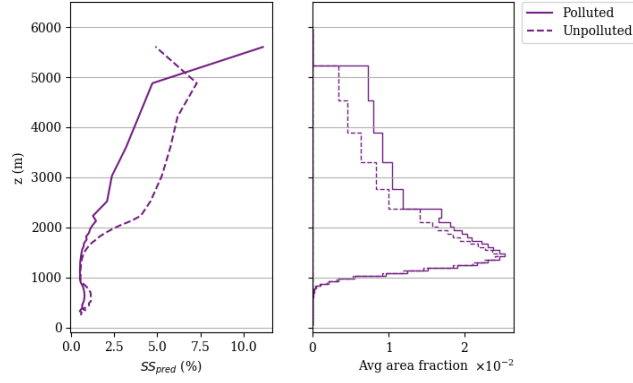
Actual versus approximated supersaturation - WRF Polluted



(b) Polluted case.

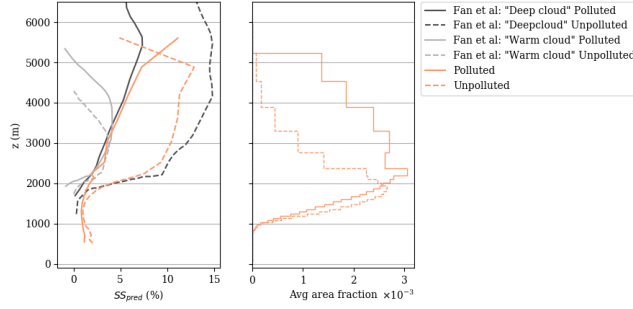
Figure 14: Same as Figure 11, without contributions from rain drops. Correlation is slightly lower and the value of least-squared linear regression slopes is lower for both simulation cases.

Supersaturation and area fraction vertical profiles - WRF Unpolluted



(a)

Supersaturation and area fraction vertical profiles - WRF Unpolluted



(b)

Figure 15: Analogous to Figure 3, restricted to the horizontal subdomain indicated by the red box in Figure S8 of Fan et al (bottom left panel). Qualitatively the results are quite similar, suggesting that the restriction to this subdomain is not crucial to the results described in Fan's paper.

References

- [1] J. Fan, D. Rosenfeld, Y. Zhang, S. E. Giangrande, Z. Li, L. A. T. Machado, S. T. Martin, Y. Yang, J. Wang, P. Artaxo, H. M. J. Barbosa, R. C. Braga, J. M. Comstock, Z. Feng, W. Gao, H. B. Gomes, F. Mei, C. Pöhlker, M. L. Pöhlker, U. Pöschl, and R. A. F. de Souza, “Substantial convection and precipitation enhancements by ultrafine aerosol particles,” *Science*, vol. 359, pp. 411–418, 1 2018.
- [2] W. W. Grabowski and H. Morrison, “Do ultrafine cloud condensation nuclei invigorate deep convection?,” *Journal of the Atmospheric Sciences*, vol. 77, pp. 2567–2583, 7 2020.
- [3] W. W. Grabowski and D. Jarecka, “Modeling condensation in shallow non-precipitating convection,” *Journal of the Atmospheric Sciences*, vol. 72, pp. 4661–4679, 12 2015.
- [4] W. A. Hoppel, G. M. Frick, and J. W. Fitzgerald, “Deducing droplet concentration and supersaturation in marine boundary layer clouds from surface aerosol measurements,” *Journal of Geophysical Research: Atmospheres*, vol. 101, pp. 26553–26565, 11 1996.
- [5] F. Yang, R. McGraw, E. P. Luke, D. Zhang, P. Kollias, and A. M. Vogelmann, “A new approach to estimate supersaturation fluctuations in stratocumulus cloud using ground-based remote-sensing measurements,” *Atmospheric Measurement Techniques*, vol. 12, pp. 5817–5828, 11 2019.
- [6] M. Koike, N. Takegawa, N. Moteki, Y. Kondo, H. Nakamura, K. Kita, H. Matsui, N. Oshima, M. Kajino, and T. Y. Nakajima, “Measurements of regional-scale aerosol impacts on cloud microphysics over the east china sea: Possible influences of warm sea surface temperature over the kuroshio ocean current,” *Journal of Geophysical Research: Atmospheres*, vol. 117, pp. n/a–n/a, 9 2012.
- [7] M. K. Politovich and W. A. Cooper, “Variability of the supersaturation in cumulus clouds,” *Journal of the Atmospheric Sciences*, vol. 45, pp. 1651–1664, 6 1988.
- [8] N. Moteki, T. Mori, H. Matsui, and S. Ohata, “Observational constraint of in-cloud supersaturation for simulations of aerosol rainout in atmospheric models,” *npj Climate and Atmospheric Science*, vol. 2, 12 2019.
- [9] H. Siebert and R. A. Shaw, “Supersaturation fluctuations during the early stage of cumulus formation,” *Journal of the Atmospheric Sciences*, vol. 74, pp. 975–988, 4 2017.
- [10] C. Shen, C. Zhao, N. Ma, J. Tao, G. Zhao, Y. Yu, and Y. Kuang, “Method to estimate water vapor supersaturation in the ambient activation process using aerosol and droplet measurement data,” *Journal of Geophysical Research: Atmospheres*, vol. 123, 9 2018.

- [11] E. Hammer, N. Bukowiecki, M. Gysel, Z. Jurányi, C. R. Hoyle, R. Vogt, U. Baltensperger, and E. Weingartner, “Investigation of the effective peak supersaturation for liquid-phase clouds at the high-alpine site jungfraujoch, switzerland (3580 m a.s.l.),” *Atmospheric Chemistry and Physics*, vol. 14, pp. 1123–1139, 1 2014.
- [12] X.-Y. Li, G. Svensson, A. Brandenburg, and N. E. L. Haugen, “Cloud-droplet growth due to supersaturation fluctuations in stratiform clouds,” *Atmospheric Chemistry and Physics*, vol. 19, pp. 639–648, 1 2019.
- [13] M. Wendisch, U. Pöschl, M. O. Andreae, L. A. T. Machado, R. Albrecht, H. Schlager, D. Rosenfeld, S. T. Martin, A. Abdelmonem, A. Afchine, A. C. Araùjo, P. Artaxo, H. Aufmhoff, H. M. J. Barbosa, S. Borrmann, R. Braga, B. Buchholz, M. A. Cecchini, A. Costa, J. Curtius, M. Dollner, M. Dorf, V. Dreiling, V. Ebert, A. Ehrlich, F. Ewald, G. Fisch, A. Fix, F. Frank, D. Fütterer, C. Heckl, F. Heidelberg, T. Hüneke, E. Jäkel, E. Järvinen, T. Jurkat, S. Kanter, U. Kästner, M. Kenntner, J. Kesselmeier, T. Klimach, M. Knecht, R. Kohl, T. Kölling, M. Krämer, M. Krüger, T. C. Krisna, J. V. Lavric, K. Longo, C. Mahnke, A. O. Manzi, B. Mayer, S. Mertes, A. Minikin, S. Molleker, S. Münch, B. Nillius, K. Pfeilsticker, C. Pöhlker, A. Roiger, D. Rose, D. Rosenow, D. Sauer, M. Schnaiter, J. Schneider, C. Schulz, R. A. F. de Souza, A. Spanu, P. Stock, D. Vila, C. Voigt, A. Walser, D. Walter, R. Weigel, B. Weinzierl, F. Werner, M. A. Yamasoe, H. Ziereis, T. Zinner, and M. Zöger, “Acridicon–chuva campaign: Studying tropical deep convective clouds and precipitation over amazonia using the new german research aircraft halo,” *Bulletin of the American Meteorological Society*, vol. 97, pp. 1885–1908, 10 2016.
- [14] J. R. Kulkarni, R. S. Maheskumar, S. B. Morwal, B. P. Kumari, M. Konwar, C. G. Deshpande, R. R. Joshi, R. V. Bhalwankar, G. Pandithurai, P. D. Safai, S. G. Narkhedkar, K. K. Dani, A. Nath, S. Nair, V. V. Sapre, P. V. Puranik, S. S. Kandalgaonkar, V. R. Mujumdar, R. M. Khaladkar, R. Vijayakumar, P. T. V., and G. B. N., “The cloud aerosol interaction and precipitation enhancement experiment (caipeer): overview and preliminary results,” *Current Science*, vol. 102, pp. 413–425, 2012.
- [15] R. R. Rogers and M. K. Yau, *A Short Course in Cloud Physics*. Butterworth Heinemann, 3 ed., 1989.
- [16] T. V. Prabha, A. Khain, R. S. Maheshkumar, G. Pandithurai, J. R. Kulkarni, M. Konwar, and B. N. Goswami, “Microphysics of premonsoon and monsoon clouds as seen from in situ measurements during the cloud aerosol interaction and precipitation enhancement experiment (caipeer),” *Journal of the Atmospheric Sciences*, vol. 68, pp. 1882–1901, 9 2011.
- [17] H. Pruppacher and J. Klett, *Microphysics of Clouds and Precipitation*. Springer Netherlands, 2010.

- [18] R. C. Braga, D. Rosenfeld, R. Weigel, T. Jurkat, M. O. Andreae, M. Wendisch, M. L. Pöhlker, T. Klimach, U. Pöschl, C. Pöhlker, C. Voigt, C. Mahnke, S. Borrmann, R. I. Albrecht, S. Molleker, D. A. Vila, L. A. T. Machado, and P. Artaxo, “Comparing parameterized versus measured microphysical properties of tropical convective cloud bases during the acridicon–chuva campaign,” *Atmospheric Chemistry and Physics*, vol. 17, pp. 7365–7386, 6 2017.
- [19] R. Weigel, P. Spichtinger, C. Mahnke, M. Klingebiel, A. Afchine, A. Petzold, M. Krämer, A. Costa, S. Molleker, P. Reutter, M. Szakáll, M. Port, L. Grulich, T. Jurkat, A. Minikin, and S. Borrmann, “Thermodynamic correction of particle concentrations measured by underwing probes on fast-flying aircraft,” *Atmospheric Measurement Techniques*, vol. 9, pp. 5135–5162, 10 2016.
- [20] T. Jurkat, R. Weigel, and C. Mahnke, “Private correspondence,” 2020.